Engineering the electromagnetic vacuum for controlling light with light in a photonic-band-gap microchip

Rongzhou Wang and Sajeev John
Department of Physics, University of Toronto, 60 St. George Street, Toronto, Ontario, Canada M5S 1A7
(Received 9 April 2004; published 5 October 2004)

We demonstrate a trimodal waveguide architecture in a three-dimensional (3D) photonic-band-gap (PBG) material, in which the local electromagnetic density of states (LDOS) within and adjacent to the waveguide exhibits a forklike wavelength filter characteristic. This facilitates the control and switching of one laser beam with other laser beams (~ 1 μW steady-state holding power and ~ 5 nW switching power) through mutual coherent resonant interaction with quantum dots. Two waveguide modes provide narrow spectral windows where the electromagnetic LDOS is enhanced by a factor of 100 or more relative to the background LDOS of a third air-waveguide mode with nearly linear dispersion. This "engineered vacuum" can be used for frequency-selective, atomic population inversion and switching (by coherent resonant optical pumping) of an inhomogeneously broadened collection of "atoms" situated adjacent to the waveguide channel. The "inverted" atomic system can then be used to coherently amplify fast optical pulses propagating through the third waveguide mode. This coherent "control of light with light" occurs without recourse to microcavity resonances (involving long cavity buildup and decay times for the optical field). Our architecture facilitates steady-state coherent pumping of the atomic system (on the lower-frequency LDOS peak) to just below the gain threshold. The higher-frequency LDOS peak is chosen to coincide with the upper Mollow sideband of the same atomic resonance fluorescence spectrum. The probing laser is adjusted to the lower Mollow sideband, which couples to the linear dispersion (high group velocity part) of the third waveguide mode. This architecture enables rapid modulation (switching) of light at the lower Mollow sideband frequency through light pulses conveyed by the linear dispersion mode at frequencies corresponding to the central Mollow component (lower LDOS peak). We demonstrate that LDOS jumps of order 100 can occur on frequency scales of $\Delta\omega \approx 10^{-4}\omega_c$ (where ω_c is the frequency of the jump) in a finite-size 3D photonic crystal (PC) consisting of only $10\times 10\times 20$ unit cells. When the semiconductor backbone of the PC has a refractive index of 3.5 and ω_c corresponds to a wavelength of 1.5 μm, this vacuum engineering may be achieved in a sample whose largest dimension is about 12 μm.

DOI: 10.1103/PhysRevA.70.043805 PACS number(s): 42.55.Tv, 42.50.−p, 42.70.Qs

I. INTRODUCTION

Photonic crystals are periodically ordered dielectric materials, which, in analogy to electrons in an atomic lattice, exhibit a band structure in the light spectrum. When this band structure exhibits a complete and omnidirectional gap in three dimensions (3D), the crystal is referred to as a photonic-band-gap (PBG) material. Inside the PBG, light cannot propagate, leading to some fundamentally new optical phenomena, such as the localization of light [1] and the inhibition of spontaneous emission [2]. During the past decade, a great deal of progress has taken place both theoretically and experimentally [3]. For example, three-dimensional photonic crystals with a complete band gap at 1.5 μm have been successfully fabricated using silicon on a very large scale using low cost processes [4].

In the "strong-coupling" regime of photon-atom interactions, where nonradiative extinction rates and dipolar dephasing rates are made sufficiently small, some spectacular effects are predicted to arise. One such phenomenon is the photon-atom bound state [5]. Furthermore, if the transition frequency of the atom is near a photonic band edge, the atom can be coherently driven by a pump laser beam to an almost totally inverted atomic state [6]. This kind of atomic population inversion by coherent resonant pumping cannot be realized in ordinary vacuum, where the Einstein rate equations [7] forbid such behavior in the steady-state limit.

If the above two-level atom is replaced by N identical two-level atoms, collective switching and inversion behavior are obtained [8]. Near the threshold value, the modulation intensity of the pump laser required to "switch" the atomic population decreases linearly as $1/N$. Even in the presence of dephasing interactions (which would eventually smear out the single-atom population inversion), the collective atomic population inversion remains large and sharply defined. Furthermore, under certain conditions, i.e., when the concentration of active atoms is high enough and the dephasing effects are relatively small, the statistics of the excited atoms can be strongly sub-Poissonian. Based on this type of atomic population inversion, both sub-Poissonian laser emission [8] and all-optical microtransistor action [9] have been proposed.

Considerations of all-optical transistor action have been presented over the past 30 years. In very early work, optical gain was achieved using a sodium-filled Fabry-Perot interferometer [10,11]. The idea, here, was to make use of a narrow Fabry-Perot resonance that can be shifted in frequency by pumping of a nonlinear medium within the Fabry-Perot cavity. In this manner, a small change in the pump field could switch the transmission behavior of a probe beam through the cavity. However, this method has a fundamental drawback—the switching time (cavity buildup time) has an inverse relationship to the switching intensity threshold. In

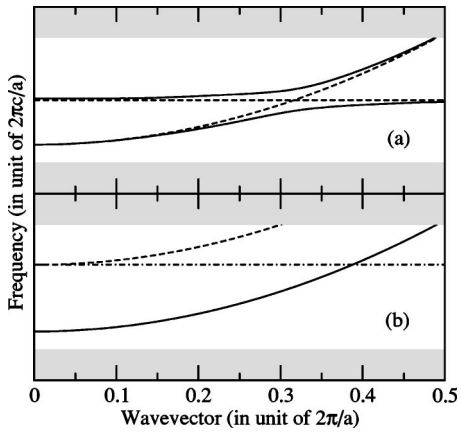

FIG. 1. Schematic picture of (a) anticrossing of a waveguide mode and a cavity mode, in which the dashed lines are the waveguide (cavity) mode with the presence of the cavity (waveguide); (b) two waveguide modes, in which the dot-dashed line indicates the cutoff frequency of the high-frequency mode. The upper and lower photonic bands are shaded to show the photonic band gaps.

other words, an intense laser beam is required to obtain a quick switch; or a slow switch is inevitable if it is operated under a weak laser beam. Similar considerations have been presented in the context of nonlinear microcavity resonators in photonic crystals [12]. Other approaches to realize all-optical transistor action have been proposed, such as by transferring the energy between the fundamental and the second-order harmonic waves [13] (cascaded second-order nonlinearities) and by photoinduced stress in semiconductors [14]. Unfortunately, these methods either require a large-size device or a high-intensity laser, which make them impractical for certain applications.

Collective atomic switching in a PBG [8], which originates from coherently induced atomic population inversion, is not constrained by the inverse relationship between switching time and switching threshold, inherent in high *Q*-factor cavity resonances. Instead, collective atomic switching requires that the local electromagnetic density of states (LDOS) exhibits a jump of order 100 over a very narrow frequency range spanning roughly one part in ten thousand of the frequency of the jump itself. In conventional photonic materials, such a large discontinuity in the LDOS is associated with a high-quality *Q*-factor microcavity resonator. For light at frequency ω_0 (corresponding to a vacuum wavelength of $\lambda = 1.5\ \mu$m), a microcavity exhibiting a large LDOS jump over the frequency scale $\Delta\omega/\omega_0 \approx 10^{-4}$ requires a cavity buildup time $\Delta\tau \geqslant 10$ picoseconds. The slowing down of light propagating in a waveguide, resonantly coupled to a microcavity, is depicted in Fig. 1(a). In the dispersion diagram for the waveguide mode, the microcavity resonance appears as a horizontal (dispersionless) line which attempts to cross the dispersion curve of the waveguide. The interaction between the localized cavity mode and the extended waveguide mode leads to a local distortion (also known as level repulsion or anticrossing) of the waveguide group velocity on resonance. In contrast, a multimode waveguide (with no coupling to a microcavity) can provide a large LDOS jump when one of the waveguide modes exhibits a cutoff [see Fig. 1(b)]. This does not require direct mode coupling and disruption of high group velocity in the first waveguide mode near the cutoff frequency of the second mode. Waveguide cutoffs in conventional dielectric waveguides typically do not achieve the required LDOS contrast because of the overwhelming presence of the background free-space density-of-states continuum $\rho(\omega) = \omega^2/(\pi^2 c^3)$ [15]. In hollow metallic waveguides [16], it is possible to expel the free-space density of states. However, the jump in the LDOS between the lowest waveguide mode and the next waveguide mode is limited by resistive losses in the walls of the waveguide channel. While large jumps may arise in a frequency range compatible with the superconducting gap of the metal, it is practically impossible to achieve the required LDOS jump at near infrared (1.5 μm) or visible frequencies. Moreover, it is impractical to couple these waveguide modes to resonant two-level atoms.

Unlike a classical high-*Q* microcavity that requires significant buildup time for light to enter and exit, an atom is a quantum resonator which absorbs and emits single photons from and to an optical mode containing *n* photons with a rate proportional to *n* [7]. Moreover, if *N* identical and equivalently situated atoms experience the same optical field, even the spontaneous-emission rate of a single photon from the atomic system is enhanced by a factor of *N* [17]. These facts facilitate ultrafast response of an atomic system to rapid modulations in an optical driving field. Moreover, rapid transfer of energy from one optical beam or pulse to another pulse can be mediated by the atoms. We suggest that with suitable mode engineering in a PBG material, this provides the possibility of ultrafast control of light with light with a relatively low power ($\sim 1\ \mu$W) holding laser beam and low-power (~ 10 nW) laser pulses that modulate the steady-state coherent pump [18].

In practice, quantum dots (instead of the two-level atoms) may be more suitable for an optical transistor device. Recently, experimental techniques to grow and precisely position quantum dots on structured semiconductor surface have emerged [19]. It may also be possible to integrate quantum dots into a PBG heterostructure [20], either within a 2D microchip layer sandwiched above and below by 3D PBG cladding or as an additional thin, solid membrane layer between the 2D microchip layer and one of the 3D PBG cladding layers.

In practice, an ensemble of quantum dots will exhibit an inhomogeneously broadened atomic resonance frequency. Although a weak inhomogeneous broadening may improve the switching characteristics by enlarging the spectral range over which the switching occurs, a strong inhomogeneous broadening hinders the overall switching effect because a large number of atoms (improperly detuned for the coherent pump frequency) may remain in the absorbing rather than amplifying state. One possible solution is to design a fork-shaped LDOS to produce a filter effect [21]. Atoms detuned from the prescribed LDOS cannot couple to either the external fields or the electromagnetic (vacuum) reservoir, and as a result the deleterious part of the atomic distribution is quenched.

The 3D photonic band gap provides the most versatile environment in which to engineer the electromagnetic

LDOS. Within the PBG, the LDOS is zero. This provides a "blank page" to design the required LDOS by introducing defects into the structure. Various kinds of defects, such as point defects, line defects, and planar defects, have been investigated [3]. Line defects (waveguides) in 2D photonic crystals have been intensively studied because of their potential to mold the flow of light in planar microcircuits [22]. However, in 2D slab and membrane photonic crystals, significant attenuation of the guided optical signal occurs due to leaky modes into the third dimension and the propensity of weak disorder to induce small-angle forward scattering into the third dimension. Moreover, the electromagnetic LDOS is dominated by the free-space 3D continuum above and below the 2D membrane.

Recently, a 3D photonic-band-gap heterostructure has been introduced which overcomes the limitation of the 2D photonic crystal, while retaining the design flexibility of a planar optical microchip [20]. In addition to facilitating "diffractionless flow of light" in waveguide circuits over a large (150 nm) bandwidth, this architecture provides an unprecedented opportunity for vacuum LDOS engineering within the optical microchip.

The band structure of the heterostructure with semi-infinite 3D PBG cladding regions (above and below the 2D microchip layer) is calculated by the plane-wave expansion method [23] as well as the supercell method [24]. The waveguide mode frequencies are shown to be adjustable by the thickness of the 2D microchip layer and the radii of rods inside the 2D microchip. Near the cutoff frequency (ω_c), the group velocity of light approaches zero, leading to a square-root divergence in the LDOS in an infinite sample. This divergence of the LDOS is interrupted by either the finite size of the sample or the finite length of the engineered waveguide section. We demonstrate that the desired forklike shape LDOS can be engineered using a trimodal waveguide architecture in a PBG microchip using suitable cutoff frequencies for two of the three waveguide modes.

The LDOS of a photonic crystal is proportional to the energy emitted by an oscillating dipole [25,26]. When a dipole emitter is inside a finite structure, the spontaneous-emission rate is calculated by integrating the electromagnetic energy flux on a surface surrounding the dipole using the finite-difference time-domain (FDTD) method [27,28].

The paper is organized as follows. In Sec. II, we review the conceptual basis of atomic switching near an LDOS discontinuity. In Sec. III, the band structure of a waveguide-engineered 3D heterostructure is calculated. The LDOS of the waveguide-engineered 3D heterostructure is presented in Sec. IV. In Sec. V, 2D photonic crystal engineering is used to discuss the desired fork-shaped LDOS. Finally, a summary is presented in Sec. VI.

II. OPTICAL SWITCHING OF DRESSED ATOMS IN AN ENGINEERED VACUUM

Here we briefly review the mechanism of the population inversion of two-level atoms in an engineered vacuum using a near-resonant classical laser field. The details can be found elsewhere [6,8,9]. When a coherent laser beam interacts with a two-level atom, the Hamiltonian of the system has the form $H=H_0+H_{AR}+H_{AL}$. The noninteracting Hamiltonian of the bare atomic and the photonic reservoir is $H_0=\hbar\Delta_{AL}\sigma_3+\Sigma_\lambda\hbar\Delta_\lambda a_\lambda^\dagger a_\lambda$, where $\Delta_{AL}=\omega_A-\omega_L$, $\Delta_\lambda=\omega_\lambda-\omega_L$, ω_A is the transition frequency of the two-level atom, ω_L is the frequency of the laser field, and ω_λ is the frequency of a mode λ. The interaction between the atom and photonic reservoir is $H_{AR}=i\hbar\Sigma_\lambda g_\lambda(a_\lambda^\dagger\sigma_{12}-\sigma_{21}a_\lambda)$ and the interaction between the atomic system and laser field is $H_{AL}=\hbar\epsilon(\sigma_{12}+\sigma_{21})$. Here $\sigma_{ij}=|i\rangle\langle j|(i,j=1,2)$ are the atomic excitation and deexcitation operators, and $\sigma_3=\sigma_{22}-\sigma_{11}$ is the atomic inversion operator. The coupling constant (g_λ) describes the coupling between the atom and the reservoir λ mode. The resonant Rabi frequency $\epsilon=\boldsymbol{\mu}\cdot\mathbf{E}/\hbar$ describes the interaction between the atom and the laser field, where $\boldsymbol{\mu}$ is the dipole moment of the atom and $\mathbf{E}$ is the applied laser field amplitude.

The Hamiltonian can be simplified by introducing the dressed atomic states $\{|\tilde{1}\rangle,|\tilde{2}\rangle\}$, defined by $|\tilde{1}\rangle=c|1\rangle+s|2\rangle$ and $|\tilde{2}\rangle=-s|1\rangle+c|2\rangle$, that diagonalize H_0+H_{AL}. Here, $c^2\equiv\cos^2(\phi)\equiv[1+\mathrm{sgn}(\Delta_{AL})|\Delta_{AL}|/(2\Omega)]/2$ and $s^2\equiv\sin^2(\phi)\equiv[1-\mathrm{sgn}(\Delta_{AL})|\Delta_{AL}|/(2\Omega)]/2$, where the generalized Rabi frequency is defined by $\Omega\equiv\sqrt{\epsilon^2+\Delta_{AL}^2/4}$. In the dressed-state basis, the total Hamiltonian becomes $H=\tilde{H}_0+\tilde{H}_I$. Here, $\tilde{H}_0=\Sigma_\lambda\hbar\Delta_\lambda a_\lambda^\dagger a_\lambda+\hbar\Omega\tilde{\sigma}_3$, and $\tilde{H}_I=i\hbar\Sigma_\lambda g_\lambda[a_\lambda^\dagger(cs\tilde{\sigma}_3+c^2\tilde{\sigma}_{12}-s^2\tilde{\sigma}_{21})]+\mathrm{H.c.}$, where $\tilde{\sigma}_{ij}=|\tilde{i}\rangle\langle\tilde{j}|(i,j=1,2)$ are the dressed atomic excitation and deexcitation operators, and $\tilde{\sigma}_3=\tilde{\sigma}_{22}-\tilde{\sigma}_{11}$ is the dressed inversion operator. Then we introduce the time-dependent interaction picture generated by the unitary operator $U\equiv\exp(-i\tilde{H}_0t)$. The interaction Hamiltonian becomes $\tilde{H}_I(t)\equiv U\tilde{H}_IU^\dagger$, where $\tilde{H}_I(t)=i\hbar\Sigma_\lambda g_\lambda[a_\lambda^\dagger(cs\tilde{\sigma}_3e^{i\Delta_\lambda t}+c^2\tilde{\sigma}_{12}e^{i(\Delta_\lambda-2\Omega)t}-s^2\tilde{\sigma}_{21}e^{i(\Delta_\lambda+2\Omega)t})]+\mathrm{H.c.}$

When the laser field amplitude (described by $\hbar\epsilon$) is strong enough so that the Mollow frequencies ω_L, $\omega_L-2\Omega$, and $\omega_L+2\Omega$ are pushed way from the DOS discontinuities, the Mollow spectral components at $\omega_L\pm2\Omega$ experience very different densities of states and can be described by spontaneous emission decay rates $\gamma_\pm=2\pi\Sigma_\lambda g_\lambda^2\delta(\omega_\lambda-\omega_L\mp2\Omega)$.

The steady-state solution of the expectation value of the inversion operator is (see Ref. [9] for details) $\langle\tilde{\sigma}_3\rangle^{st}=(\gamma_-s^4-\gamma_+c^4)/(\gamma_-s^4+\gamma_+c^4)$. For the case $\Delta_{AL}>0$, coefficient $c^2>s^2$. The dressed state $|\tilde{2}\rangle$ is mostly comprised of the bare excited state $|2\rangle$. When $\gamma_-s^4>\gamma_+c^4$, the dressed state $|\tilde{2}\rangle$ is more populated in the steady-state regime, which corresponds to an accumulation of atomic population on the bare excited state $|2\rangle$. In other words, at a pump intensity threshold, ϵ_{thr}, defined by the condition $\tan^4\phi=\gamma_+/\gamma_-$, the atom switches from being in an absorptive state on the lower Mollow sideband at frequency $\omega_L-2\Omega$ to one that provides gain to an optical pulse at the same frequency. In the absence of any LDOS jump (i.e., $\gamma_+=\gamma_-$), we recapture the atomic population behavior predicted by the Einstein rate equations. Namely, it is impossible to achieve population inversion by coherent resonant pumping. Unlike population inversion in conventional lasers, achieved by incorporating additional level structure into the atom (i.e., three- or four-level atoms), population inversion in the context of our two-level atom is achieved by incorporating nontrivial structure into the

vacuum. Moreover, the steady-state atomic switching occurs through entirely coherent processes. The larger the LDOS jump (as determined by the ratio γ_+/γ_-), the lower the switching threshold. Moreover, it has been shown that for a collection of N indistinguishable atoms, the width of the switching intensity regime (corresponding to the required intensity of a pump pulse over and above a steady-state pump "holding field") is proportional to $1/N$.

As argued in Ref. [18], when the PBG waveguide architecture provides a factor of 100 jumps of the LDOS over the frequency range of 1–10 GHz, a 100 nW continuous laser beam passing through a micron-scale waveguide channel, with suitable field enhancement effects in certain locations, is sufficient to induce steady-state atomic inversion at those locations. The precise relation between peak electric-field amplitudes and power passing through a waveguide channel depends sensitively on the precise photonic crystal architecture. A 100 nW continuous-wave laser beam guided through a waveguide channel of cross section 1 μm by 1 μm produces an average intensity of 10 W/cm^2. However, in a real photonic crystal waveguide, the field intensity is not uniform over the cross section of the waveguide, but highly concentrated in specific regions (see Fig. 4). The intensity in these "hot spots" can be more than 10 times the average. If the quantum dots are placed in these specific (periodically repeating) "hot spots," the effective Rabi frequency associated with a 50–100 nW laser beam can be in the 10–20 GHz range. In the present paper, we describe specific photonic crystal waveguide architectures that approach these earlier estimates. Moreover, the quantum dots, placed in these optically equivalent positions, are expected to respond collectively (i.e., as though they were confined to the same cubic half-wavelength region of space). By spreading the "atomic" system over the length of the trimodal waveguide channel ($\gtrsim 10$ μm), the atom-field interaction is expected to be dominant compared to direct resonance dipole-dipole interaction between the atoms.

As can be seen from the above expressions, the atomic switching process depends on the detuning, Δ_{AL}, of the atomic resonance frequency from the pump laser frequency. In an inhomogeneously broadened atomic distribution, improperly detuned atoms will continue to be in an absorbing state, thereby offsetting the gain provided by other atoms that have undergone switching. It is the aim of the remainder of this paper to demonstrate that (i) LDOS engineering can be performed in a 3D PBG optical microchip to achieve very large LDOS jumps, γ_+/γ_-, over very narrow frequency intervals ($\lesssim\Omega$), and (ii) additional LDOS engineering can be implemented to retain only relevant parts of inhomogeneously broadened atomic distribution that contribute to gain at a particular pump intensity, ϵ, whereas improperly detuned atoms in the same distribution can be quenched (prevented from absorbing and decoupled from the electromagnetic reservoir).

III. BAND STRUCTURE OF A MULTIMODE WAVEGUIDE 3D PBG HETEROSTRUCTURE

Our architecture for controlling light with light consists of three parts: upper and lower cladding sections, consisting of 3D PBG material, sandwiching a lattice-matched 2D photonic crystal chip, as depicted in Fig. 2. Within the microchip layer, optical air-waveguide channels are created by removing one or more lines of dielectric rods. For concreteness, we consider rods adjacent to the waveguide channel that contain two-level atoms (quantum dots). We evaluate, in this paper, the LDOS profiles in the vicinity of such light emitters.

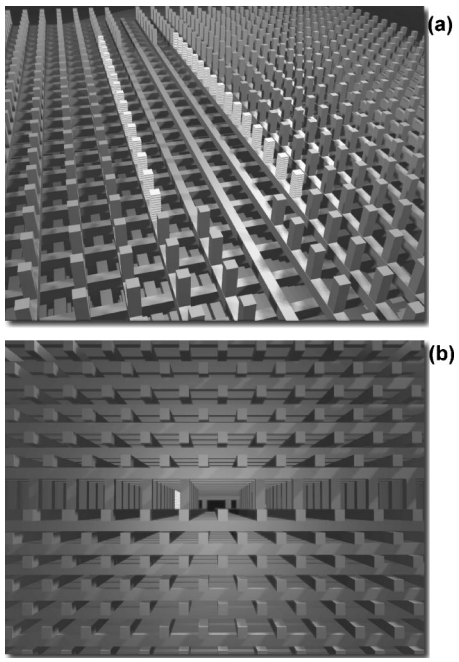

FIG. 2. The heterostructure with woodpile structure as the upper and lower 3D PBG cladding sections. The middle part is a W3 waveguide with highlighted rods in which quantum dots (or two-level atoms) are integrated. The ends of the W3 waveguide are connected by W1 waveguides. (a) Bird's eye view with the upper cladding section removed. (b) Side view with both upper and lower cladding sections.

The upper and lower 3D PBG cladding material can consist of any structure with a large 3D photonic band gap, such as inverse square spirals [29], woodpiles [30], slanted pores [31], etc. The middle part is a lattice-matched 2D photonic crystal slab with a waveguide created by removing one or more lines of a dielectric rod. The structure with one line (three lines) of rods removed is denoted as a W1 (W3) waveguide. The 2D slab plane is chosen as the xy plane with the waveguide along the y direction, and the direction perpendicular to the 2D slab is the z direction.

For concreteness, inverse square spiral structures [20,29] are used as 3D PBG material cladding sections. They have a lattice constant a along the x and y axes, and $1.7a$ along the z axis. The structure consists of spiral air arms that interleave in silicon (dielectric constant 11.9): the transverse arm length is $1.5a$ and the circular cross section is $0.33a$. This photonic crystal has a PBG to a center frequency ratio of about 24% [29]. The intercalated 2D PC slab consists of silicon rods arranged in a square lattice with lattice constant a and rod radius 0.17a. The height (h) of the 2D slab (along the z direction) is $0.4a$. For light of wavelength near 1.5 μm providing the "atomic" switching, the 2D lattice constant is a

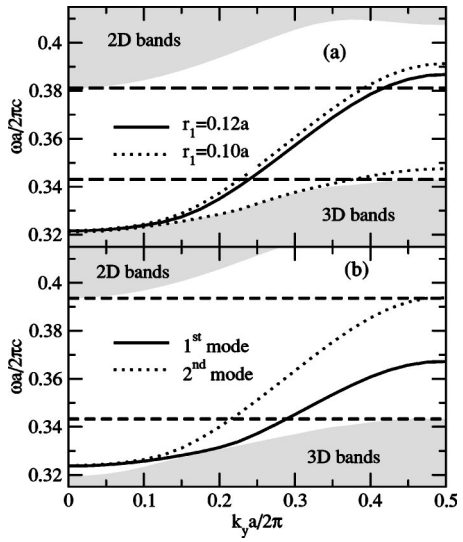

FIG. 3. Band structure of (a) W1 heterostructure when $h=0.4a$, and $r_1=0.12a$; (b) W3 heterostructure when $h=0.3a$, and $r_1=0.12a$. Shaded areas are 2D and 3D bands, respectively. The on-chip PBG is shown by dashed lines. The group velocity of the second mode at the cutoff frequency of the first mode is $0.24c$, where c is the speed of light in the vacuum.

≈ 600 nm and the thickness of the microchip layer is $h \approx 250$ nm. The detailed precess of fabricating this heterostructure is described in Ref. [20]. We emphasize, however, that this serves only as a concrete illustration. The concepts described in the present paper can equally well be applied to nearly any 3D PBG material and its associated 2D-3D microchip heterostructure [20].

The evaluation of the electric-field amplitude in a supercell of the 2D-3D PBG heterostructure (using plane-wave expansion) is described in Appendix A. The supercell is chosen to be as follows: In the x direction, there are five unit structures on each side of the waveguide, i.e., $11a$ ($13a$) for the W1 (W3) waveguide. In the y direction, there is only one unit. In the z direction, there are three unit layers of the inverse spiral structure both above and below the 2D slab, i.e., the height of the waveguide supercell along the z direction is $1.7a\times 3+h+1.7a\times 3=10.2a+h$, where h is the height of the 2D slab. Plane waves satisfying $|G|\leqslant 2.5(2\pi/a)$ are used in the field mode expansion. This corresponds to (i) using 4427 plane waves for the W1 waveguide when $h=0.4a$; (ii) using 5187 plane waves for the W3 waveguide when $h=0.4a$; and (iii) using 5147 plane waves for W3 waveguide when $h=0.3a$.

The band structure of the W1 heterostructure is given in Ref. [20]. The relevant features are summarized below. When there is no on-chip waveguide inside the intercalated 2D microchip, some 2D planar waveguide bands [upper shaded regions in Figs. 3(a) and 3(b)] will occupy the upper fraction of the original 3D PBG. However, a complete on-chip 3D PBG is retained [unshaded region between horizontal dashed lines in Figs. 3(a) and 3(b)] below these planar modes. The size of this on-chip band gap decreases with the thickness of the 2D microchip layer, disappearing completely if the thickness is $0.8a$. Meanwhile, removing one line of rods in the 2D microchip will create a linear air-waveguide (W1) mode inside the on-chip band gap. The bandwidth of this single-mode waveguide also depends sensitively on the thickness of the 2D microchip. Light localization by the PBG materials surrounding this air waveguide enables flow of light without diffraction through micron-scale bends in air. It was found [20] that when the thickness of the 2D microchip is $0.5a$, the single-mode region of diffractionless light flow is about 130 nm (for a band centered at 1.55 μm). However, the defect mode can be further engineered by modifying the radius (r_1) of rods adjacent to the air waveguide. As shown in Fig. 3(a), when r_1 decreases, the waveguide mode within the on-chip 3D PBG is raised in frequency. Here, the decreasing of r_1 decreases the total amount of dielectric material in the 2D microchip. By adjusting the thickness of the 2D microchip to $0.4a$ and r_1 to $0.12a$, the single-mode region increases from about 130 nm to 160 nm (for a band centered at 1.55 μm).

When the wave vector $k_y=0.5(2\pi/a)$, the W1 mode exhibits a sharp frequency cutoff. In a 3D photonic crystal, a local maximum or minimum frequency in the band corresponds to a peak in the DOS at that frequency. However, in an infinite one-dimensional waveguide, this peak is in fact a divergence in the LDOS: Near the cutoff frequency, the waveguide mode dispersion relation can be approximated by a parabolic function, i.e., $\omega=\omega_c-A(k_y-k_c)^2$, where k_c is the wave vector corresponding to ω_c and A is a fitting constant. Consequently, the photon DOS will be $\rho_1(\omega)=(1/2)A(\omega_c-\omega)^{-1/2}$, which is divergent at ω_c. However, in practice, the size of the heterostructure (and length of the corresponding waveguide) is always finite. As a result, the LDOS divergence is replaced by a large but finite discontinuity near the cutoff frequency. Nevertheless, this architecture provides the maximal contrast, γ_+/γ_-, over the narrowest possible frequency interval, as required for low threshold atomic switching.

Near the cutoff frequency of the waveguide mode described above, the group velocity vanishes. As a result, this mode is useful for carrying a steady-state "holding" laser field that pumps ("biases") the atomic system to just below a specified, switching threshold. Due to the long buildup time in this slow mode, it cannot be used for rapid modulation of the pump from below to above the switching threshold. For modulation, a second high group velocity mode ("gate") is required. This second waveguide mode can also be used for sending a rapid stream of data (modulated intensity) that "probes" the pumped atomic system. Depending on the state of the atomic system (as determined by the bias and gate optical fields), the probe pulses can be amplified or attenuated. An additional linear dispersion waveguide mode for the probe and gate optical fields can be engineered by removing three lines of rods from the 2D photonic crystal slab (W3 waveguide). In practice, the W3 waveguide may be engineered as a short (20 unit cells) segment of a longer W1 waveguide. In order to avoid scatterings and Fabry-Perot resonance effects at the boundary between W1 and W3 waveguides, a gradual reduction of the adjacent rod size of a W1 waveguide to zero may be very efficacious.

The band structure for a W3 heterostructure is plotted in Fig. 3(b). There are two waveguide modes inside the on-chip

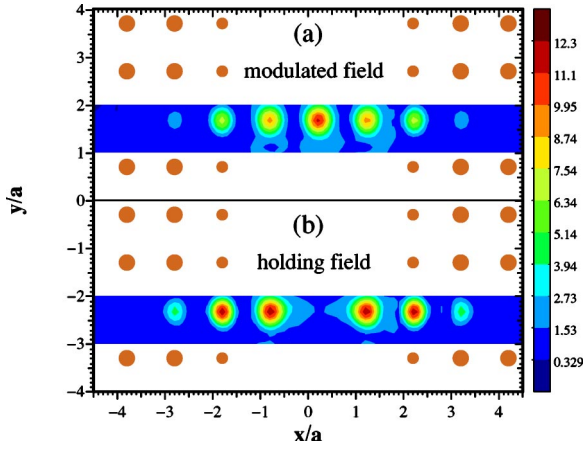

FIG. 4. Electric field distributions of the W3 structure with $h=0.3a$, and $r_1=0.12a$, on the $z=0$ plane for (a) the second (group velocity of about $0.25c$) waveguide mode at $\mathbf{k}=(0,0.3,0)(2\pi/a)$, where the corresponding frequency is near the cutoff frequency of the second (holding field) waveguide mode; (b) the first (zero group velocity) waveguide mode at $\mathbf{k}=(0,0.5,0)(2\pi/a)$. The y axis is shifted to plot the figure. The shaded circles are 2D dielectric rods.

band gap, which are called the first (with a lower frequency) and the second (with a higher frequency) mode in the following text. By changing the thickness of the 2D microchip to $0.3a$, the on-chip band gap can be enlarged. Meanwhile, the cutoff frequency of the first mode can be tuned to the middle of the on-chip 3D PBG. This adjustment of the on-chip PBG and the position of the cutoff frequency help make the structure robust to some forms of disorder introduced during the fabrication process.

Near the cutoff frequency of the first mode (ω_c), the frequency of the second mode depends almost linearly on the wave vector k_y. The group velocity of the second mode near the cutoff frequency of the first mode is $0.24c$, where c is the speed of light in the vacuum. Since the cutoff frequency is inside the band gap, no other modes contribute to the photon DOS in the vicinity of ω_c, i.e., the photon DOS near the cutoff frequency of the lower waveguide mode is the sum of only two modes: $\rho(\omega)=\rho_1(\omega)+\rho_2(\omega)$, where 1 (2) stands for the first (second) waveguide mode. The first term $\rho_1(\omega) \propto(\omega_c-\omega)^{-1/2}$ is divergent at ω_c, whereas $\rho_2(\omega)$ remains relatively small near ω_c. The total effect is a LDOS peak superimposed on a weak, nearly constant background.

The electric-field distributions of the waveguide modes at the $z=0$ (middle of the 2D microchip) plane are plotted in Fig. 4. Since the electric fields are mostly parallel to the z direction, i.e., electric fields are perpendicular to the 2D slab plane, only the z components of the fields are shown here. Almost all the fields are localized near the waveguide (near $x=0$). Away from the air waveguide, the fields concentrate on the adjacent dielectric rods. To enhance the interaction between the quantum dots and the field, the quantum dots can be placed in multiple layers inside these rods adjacent to the air waveguide or above and below the 2D microchip layer near the air waveguide.

Near the cutoff frequency of the defect mode, the wave vector is almost $k=(0,0.5,0)(2\pi/a)$, which means the phase angle of the field will change by π from one unit cell to the next along the waveguide, i.e., the field intensity will be almost the same for each unit cell along the waveguide direction. This is helpful to achieve collective switching behavior when a large number of atoms (or quantum dots) are distributed over equivalent, periodically repeating positions.

We estimate the power of the pump laser beam passing through the waveguide in Fig. 4 to realize atomic population inversion. The Rabi frequency can be obtained by the formula $|\Omega|=2.2\times10^8\sqrt{I[\mathrm{W/cm^2}]}|\mathbf{d}\cdot\mathbf{e}|/(ea_0)$ [33], where $I\equiv(c/8\pi)|\mathbf{E}|^2$ is the intensity of the laser beam in units of $\mathrm{W/cm^2}$, $|\mathbf{E}|$ is the electric-field amplitude, $|\mathbf{d}\cdot\mathbf{e}|$ is the projection of the dipole moments in the electric-field direction, e is the electron charge, and a_0 is the Bohr radius. Usually, $|\mathbf{d}\cdot\mathbf{e}|\sim0.1-10(ea_0)$. When $|\mathbf{d}\cdot\mathbf{e}|=10(ea_0)$ and the light wavelength is 1.5 μm, one nanometer shift (133 GHz shift) of a Mollow sideband from the central frequency of the Mollow spectrum requires an electric amplitude of about 10^4 V/cm at the location of the atom (quantum dot). If a jump within $10^{-4}\omega_c$ is achieved in the DOS (0.15 nm or 20 GHz shift for $\lambda=1.5$ μm), the laser electric amplitude required for atomic switching in the simple model (the single two-level-atom case) of Sec. II is about 1.6×10^3 V/cm. Although the electric-field amplitudes required for atomic switching are moderate, the total energy and power requirement for switching are very small due to the submicron-scale confinement of the optical fields within a typical photonic-band-gap waveguide geometry. For a PBG centered near 1.5 μm, the required photonic crystal lattice constant $a\sim0.4\lambda\approx600$ nm. One unit volume of the waveguide direction is about $5a\times0.3a\times1a\approx0.3$ $(\mu\mathrm{m})^3$. The energy stored along one unit cell of the waveguide channel, at the atomic switching threshold, is about 0.6×10^{-11} nJ for the zero group velocity mode (first mode) in Fig. 4(b) or 1×10^{-11} nJ for the high group velocity mode (second mode) in Fig. 4(a). In Fig. 4, it is suggested that the steady-state holding field passes through the zero group velocity mode (b) and pumps quantum dots in the adjacent rods. In this case, there is no net power flow in the holding field, and small modulations in a weaker pump field passing through the high group velocity mode (a) enable collective "atomic" switching of the adjacent Q dots between absorbing and amplifying states. An alternative pumping mechanism is to require both the steady-state holding field and the weaker modulation field to pass through the high group velocity mode (b). In the latter scenario, the power of the holding field (near switching threshold) can be estimated as the mode group velocity ($\approx0.25c$) multiplied by the energy contained per unit length along the waveguide direction. In this case, the required power for switching is about 1 μW. When a large (~1000) number of quantum dots responds collectively, the amplitude of the switching laser is about 5% of the holding field amplitude. In this case, the power of the modulating pump laser passing through the high group velocity (linear dispersion) waveguide mode can be 3 nW, provided that the steady holding laser intensity is just below the switching threshold.

IV. THE LOCAL DENSITY OF STATES NEAR A MULTIMODE WAVEGUIDE IN A 3D PBG HETEROSTRUCTURE

The local electromagnetic density of states (LDOS) is defined as

$$\rho(\omega,\mathbf{r}_0)=\frac{1}{\mathcal{V}d_0^2}\sum_n |\mathbf{d}\cdot\mathbf{E}_n^{(T)*}(\mathbf{r}_0)|^2\delta(\omega-\omega_n^{(T)}), \tag{1}$$

where $\mathcal{V}$ is the volume of the structure, d_0 is the magnitude of the dipole momentum $\mathbf{d}$, and $\mathbf{E}_n^{(T)}(\mathbf{r}_0)$ is the eigenvector of the electric field (quasitransverse mode) at position $\mathbf{r}_0$ with an eigenvalue ω_n. The LDOS can be obtained from the energy U emitted from a dipole inside the structure (see Appendix B),

$$\rho(\omega,\mathbf{r}_0)=\frac{\epsilon_0}{\pi\omega^2 d_0^2}U. \tag{2}$$

To focus on the LDOS of a waveguide mode near its cutoff frequency, we study the W1 waveguide since there is only one mode near the cutoff frequency. The upper and lower cladding layers of the 2D-3D heterostructure used in this section consist of inverse square spiral photonic crystals. Each cladding layer has three unit cells in the z direction. The height of the 2D microchip layer sandwiched between the cladding layers is $0.4a$. The total height of our supercell in the z direction is $1.7a\times3+0.4a+1.7a\times3=10.6a$. In the x direction, there are five lines of rods on each side of the waveguide, i.e., the length in the x direction is $5a+a+5a=11a$. The length of the waveguide (in the y direction) is varied to determine its influence on the LDOS. Several waveguides are used, for example $7a$ in the y direction (denoted as $y7$), $9a$ in the y direction (denoted as $y9$), etc.

In order to determine the LDOS within the microchip, a dipole is placed near the center of the rod adjacent to the waveguide halfway along the length of the waveguide. The direction of the dipole is parallel to the z direction. In our numerical calculations, a cubic FDTD grid [1] is used with 10 points per lattice constant a, i.e., $\Delta x=\Delta y=\Delta z=\Delta=0.1a$. The finite-size structure is placed in vacuum, which we simulate with the second-order Mur absorbing boundary condition [34].

The LDOS of the heterostructure is shown in Fig. 5. Near the cutoff frequency (corresponding to the infinite structure), $\omega_c\approx0.38(2\pi c/a)$, there is a peak in the LDOS that becomes more pronounced as the waveguide becomes longer. As the length of the heterostructure along the y direction increases, the peak value $\rho_{\max}$ of the LDOS increases rapidly. At the same time, the peak width decreases. When the length of the waveguide goes to infinity, the peak in the LDOS will eventually become a divergent point at ω_c, as discussed in Sec. III. Below the cutoff frequency, the lowest value of the LDOS, $\rho_{\min}$, is almost the same for structures with different lengths in the y direction. This is due to the linear dispersion of the second waveguide mode near $\omega=0.36(2\pi c/a)$, as seen in Fig. 3(b).

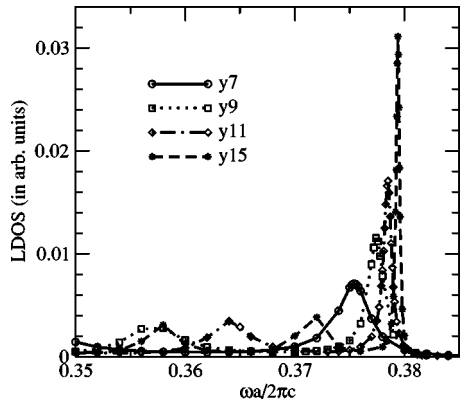

FIG. 5. The LDOS of the finite heterostructure with different length in the waveguide direction (y direction). The dipole is placed at $\mathbf{r}=(-0.7,0.3,0)a$. The origin of the coordinate is the center of the structure.

Besides the peak near ω_c, there are some smaller fringes in the LDOS when $\omega<\omega_c$ due to finite-size effects. This is a Fabry-Perot effect arising from the photonic crystal to free space boundary at the edges of our sample. Light that is reflected by the ends of the heterostructure (in the y direction that the light can propagate) exhibits constructive and destructive interference fringes along the length of the waveguide.

When the dipole is placed in the center of a waveguide ($\mathbf{x}_0$), the distance that the reflected light travels, from $\mathbf{x}_0$ to one end of the waveguide and back to $\mathbf{x}_0$, will be L (the length of the waveguide). If the field emitted by the dipole has a form of $e^{i(k_y y-\omega t)}$, the phase difference between the field emitted by the dipole and the fields reflected by the ends will be $\Delta\phi=kL$. When the wave vector k_m (corresponding to ω_m) satisfies

$$k_m L=\Delta\phi=n2\pi \quad (n=0,1,2,\ldots), \tag{3}$$

constructive interference occurs, which increases the total electric field $\mathbf{E}$ at $\mathbf{x}_0$. Since the energy emitted by the dipole is proportional to the total electric field, i.e., $U\propto|\mathbf{d}\cdot\mathbf{E}|$, U will be maximum at ω_m. Consequently, the LDOS also has a maximum value at ω_m. In Table I, some wave vectors that satisfy Eq. (3) are shown. From these wave vectors, the cor-

TABLE I. Wave vectors satisfy Eq. (3).

L	Wave vector	$\Delta\phi$	Frequency
9a	$0.33(2\pi/a)$	6π	$0.359(2\pi c/a)$
11a	$0.36(2\pi/a)$	8π	$0.365(2\pi c/a)$
15a	$0.33(2\pi/a)$	10π	$0.359(2\pi c/a)$
15a	$0.40(2\pi/a)$	12π	$0.372(2\pi c/a)$

[1] The time interval is chosen to be $\Delta t=0.95\Delta/(c\sqrt{3})$. These parameters are within the stability bound [28]. For light propagating in vacuum, more than 20 grid points per wavelength, ie., $\omega\leqslant0.5(2\pi c/a)$ if $\Delta=0.1a$, will lead to an intrinsic grid velocity anisotropy of less than 0.2%. The numerical wave propagating in vacuum will grow exponentially when $\Delta t>\Delta/(c\sqrt{3})$.

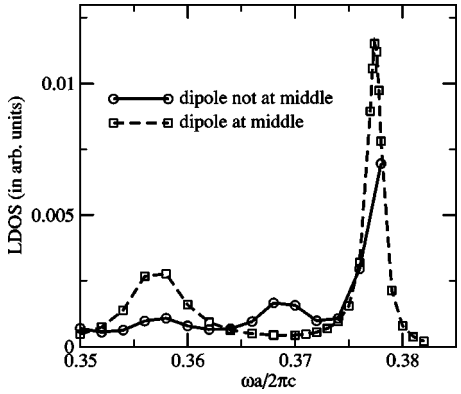

FIG. 6. The emission power when the dipole is placed at different positions inside a *y*9 structure. The line with rectangular symbols is the case in which the dipole is placed at $\mathbf{r}=(-0.7,0.3,0)a$ (same as the dash line with rectangular symbols in Fig. 5); and the line with circular symbols is the case in which the dipole is placed at $\mathbf{r}=(-0.7,-0.7,0)a$.

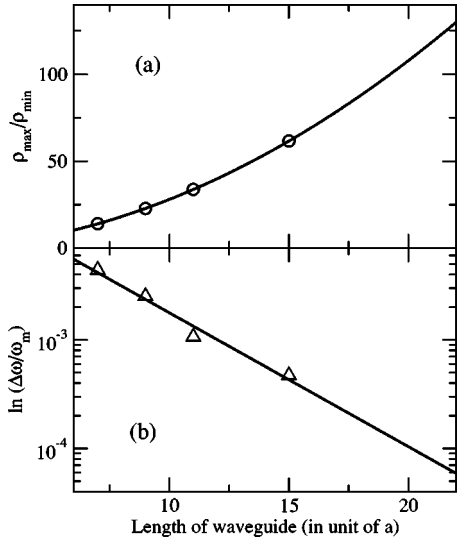

FIG. 7. Analytic functions fitted for (a) peak value and (b) peak width.

responding frequencies are obtained approximately from Fig. 3(a). Clearly, the estimated frequencies of the fringes in Table I agree well with those in Fig. 5.

When the dipole is placed away from the middle of the waveguide, the distance l that the reflected light travels will be changed. Consequently, the wave vector that satisfies the constructive interference condition is also changed. This is seen in Fig. 6, in which the secondary peaks of the LDOS change from $0.358(2\pi c/a)$ to $0.368(2\pi c/a)$. Beside the fringe near $0.368(2\pi c/a)$ in Fig. 6, there is another small fringe near the frequency of $0.358(2\pi c/a)$. The position of the fringe is the same as that when the dipole is placed in the middle of the *y*9 structure. This can be explained by the constructive interference between the light emitted by the dipole and the light reflected twice by two ends, i.e., from $\mathbf{x}_0$ to one end, then to another end, and back to $\mathbf{x}_0$. Now the distance that the reflected light travels is $l=18a$. By setting $L=18a$ in Eq. (3), we have $k=0.33(2\pi/a)$ when $n=6$. This has the same wave vector as that of the *y*9 structure in Table I. Consequently, the fringe will not change position when the dipole is placed away from the middle of the structure. Since light is reflected two times by both ends, respectively, before it interferes with the light emitted by the dipole, the reflected light will be much smaller than that reflected only once, leading to a smaller peak.

We now consider in greater detail the properties of the dominant peak arising from the waveguide cutoff. If the frequency of the peak LDOS, $\rho_{\max}$, is ω_m, and the frequency at $0.5\rho_{\max}$ (bigger than ω_m) is ω_r, the peak width is simply defined as $\Delta\omega=\omega_r-\omega_m$. For waveguides with different lengths, the peak value and peak width can be fitted to analytic functions, as shown in Fig. 7. The peak value can be fitted as $\rho_{\max}(L)/\rho_{\min}=a_0+a_1L+a_2L^2$, where a_0, a_1, a_2 are fitting parameters. Likewise, the peak width can be fitted as $\Delta\omega(L)/\omega_c=be^{-\alpha L}$. Here b, α are fitting parameters and the cutoff frequency ω_c is chosen to be $0.38(2\pi c/a)$.

The LDOS changes slowly near $\rho_{\max}$. As a result, $\rho_{\max}$ is insensitive to the location of ω_m, i.e., a small error in ω_m has little effect on the value of the LDOS. Therefore, the peak value is obtained with negligible error and it can be fitted well [see Fig. 7(a)]. In contrast, the LDOS changes quickly near $0.5\rho_{\max}$. Consequently, it is sensitive to the location of ω_r. This explains the slight deviations of the data points from the fitting function [see Fig. 7(b)]. Nevertheless, the evolution of the peak width with the length of the waveguide is clearly discernible.

Since the evaluation of the LDOS of a long waveguide by FDTD methods is very time consuming, it is useful to infer the desired properties by extrapolation. For a W3 waveguide (three missing rows of rods) suitable for atomic switching, the ratio $\rho_{\max}/\rho_{\min}$ [shown in Fig. 7(a)] describes the ratio of the peak LDOS arising from a mode cutoff to the background LDOS of a linear dispersion mode. When the length of the W3 waveguide is $20a$, the ratio $\rho_{\max}/\rho_{\min}$ is about 100, suitable for low threshold switching. Meanwhile, the LDOS peak width decreases rapidly with waveguide length. In particular, the ratio $\Delta\omega/\omega_c$ is as small as 10^{-4} when the waveguide length is $20a$.

The accuracy of our numerical FDTD results can be determined by varying the size of the grid used to represent a given unit cell. In Fig. 8, two different grid spacings, Δ, are used to calculate the LDOS of a W1 waveguide (9*y*) and compared. The dashed line with square symbols results from a coarse mesh $\Delta=a/10$, and the solid line with circular symbols results from a fine mesh $\Delta=a/20$. The peak of the LDOS exhibits a blueshift as the mesh is made finer. However, the shape of the peak and the position of the lowest-order fringe remain relatively unchanged. In our calculations, we average the dielectric constant in the discrete mesh. For light of 1.5 μm wavelength, the lattice constant $a\approx 600$ nm. In this case, the FDTD grid spacing used in Fig. 8 corresponds to 60 nm (coarse mesh) and 30 nm (fine mesh). Accordingly, our results are insensitive to surface randomness of the 2D microchip on these length scales.

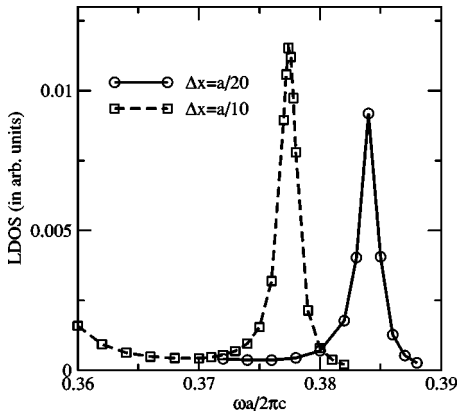

FIG. 8. Emission power calculated by the FDTD method using two different meshes.

V. DESIGN OF A LDOS FILTER FOR SWITCHING IN AN INHOMOGENEOUSLY BROADENED ATOMIC DISTRIBUTION

In the previous section, we have studied the nature of the LDOS jump in a finite-size 3D structure designed for switching of a collection of identical quantum dots. In practice, a collection of quantum dots in a real semiconductor is characterized by a size distribution, leading to an inhomogeneous broadening of the "atomic" spectrum. As described in the Introduction, such a distribution of "atomic" transitions relative to a single LDOS jump can result in a washing out of the overall switching effect. Switching depends sensitively on the detuning of the atomic transition relative to the LDOS jump and the pump laser. In this section, we introduce a new microchip architecture that provides an LDOS filter. Here, only those quantum dots whose Mollow components are driven by the external laser into resonance with prescribed peaks in the LDOS can participate in the switching process, whereas improperly detuned quantum dots are effectively removed (quenched) from strongly influencing the probe laser beam. Since the LDOS peaks have a prescribed frequency separation, this architecture also fixes the intensity (Rabi frequency) of the pump laser to cause "atomic" inversion. Our new architecture consists of a trimodal waveguide in which two waveguide modes exhibit closely spaced cutoffs and the third waveguide mode exhibits nearly linear dispersion. For simplicity, we limit our attention to a 2D photonic crystal with the understanding that the corresponding 2D microchip layer will be embedded in a 2D-3D heterostructure.

We use a square lattice with circular rods and consider only the *E*-polarization mode (electric field parallel to the rods), because the field pattern in the 3D heterostructures closely resembles the *E*-polarization mode in a 2D photonic crystal. The lattice constant is a and the radius of rods is $r_0=0.25a$. The configuration of the waveguide structure is depicted in Fig. 9. We demonstrate that this structure exhibits a forklike LDOS suitable for selecting suitably pumped "atoms" for switching, while filtering out other "atoms" from an inhomogeneously broadened distribution.

A. Band structure

To obtain the waveguide modes, the plane-wave expansion and supercell method are used. The 2D supercell contains 19 units in the x direction and 1 unit in the y direction. The expansion plane waves are chosen by $|\mathbf{G}|<8(2\pi/a)$, corresponding to 3757 plane waves. The dielectric constant of each rod is 11.9. When the rod radius (r_0) is $0.25a$, the structure has a full stop gap from $0.251-0.355(2\pi c/a)$ for the *E*-polarization mode. As plotted in Fig. 9, three rows of rods are modified to create a trimodal waveguide and the desired shape of the LDOS. By completely removing one line of rods, an air-waveguide mode is created with its lower-cutoff frequency (mode 3) near the center of the gap. By reducing the radius (r_1) of one line of rods, another waveguide mode (mode 1) is created with upper-cutoff frequency near the center of the gap. Finally, by reducing the radius (r_2) of another line of rods, we create a waveguide mode (mode 2) with a linear dispersion relation near the center of the gap. The group velocity of mode 2 near the cutoff frequencies (of mode 1 and Mode 3) is $0.24c$, where c is the light velocity in vacuum. The corresponding band structure is plotted in Fig. 10, in which $r_0=0.25a$, $r_1=0.17a$, and $r_2=0.14a$. The electric-field distributions of these waveguide modes are depicted in Fig. 11. Near the center of the rods adjacent to the air waveguide (point *P* in Fig. 9), the electric fields of all the waveguide modes are strong enough to guarantee the coupling between quantum dots and these modes for the switching behavior.

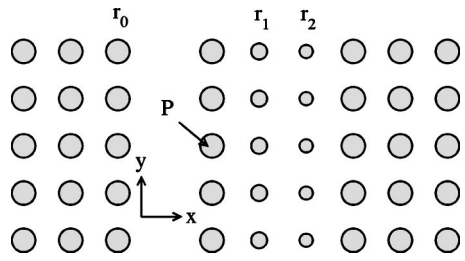

FIG. 9. Architecture for an LDOS filter for switching in an inhomogeneously broadened "atomic system." The two-level atoms or quantum dots are placed at point *P* and other equivalent points. The 2D photonic crystal has a square lattice with rod radius r_0.

The lower-cutoff frequency, ω_3, of the air waveguide (mode 3) can be adjusted by the radius, r_0, of the background 2D rods. When $r_0=0.25a$, ω_3 is near the center of the gap.

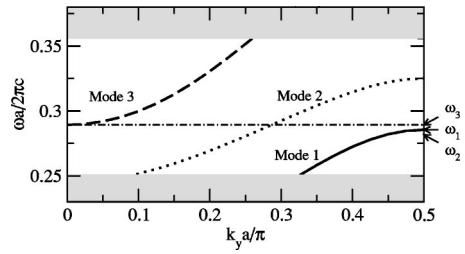

FIG. 10. The band structure of the 2D photonic crystal with three waveguide modes. Mode 1 (solid line) and mode 3 (dashed line) exhibit cutoffs within the PBG and contribute to sharp LDOS peaks, whereas mode 2 (dotted line) exhibits nearly linear dispersion in the same vicinity. The probe laser frequency (position of lower Mollow sideband) is indicated as ω_2, the pump laser frequency is indicated as ω_1, and the position of the upper Mollow sideband is indicated as ω_3.

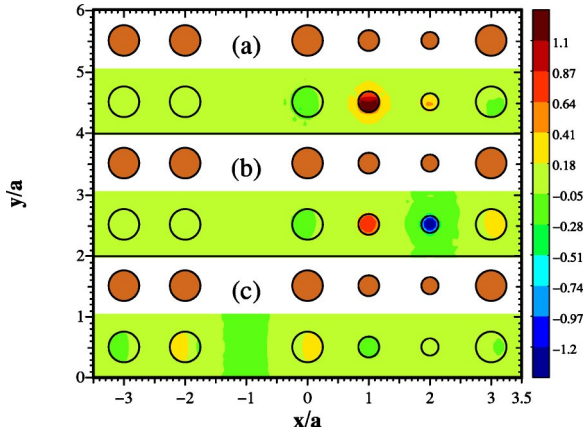

FIG. 11. Electric-field distributions of the waveguide modes in Fig. 10. (a) Mode 1 at $\mathbf{k}=(0,0)(2\pi/a)$; (b) mode 2 at $\mathbf{k}=(0,0.3)\times(2\pi/a)$; and (c) mode 3 at $\mathbf{k}=(0,0)(2\pi/a)$.

The upper-cutoff frequency, ω_1, of the waveguide (mode 1) can be adjusted by changing the rod radius r_1. The dependence of the cutoff frequencies on r_1 is plotted in Fig. 12. When r_1 increases, the cutoff frequency of the air waveguide (mode 3) is almost invariant (it actually decreases very, very slowly), while the cutoff frequency of the waveguide (mode 1) decreases noticeably. This makes the relative position between these two cutoff frequencies adjustable by changing r_1. The waveguide (mode 2) carries the probing laser and has a high group velocity ($0.24c$, see Fig. 10) enabling a quick response for ultrafast switching.

B. Local density of states

Finally, the LDOS of the waveguide architecture described by Fig. 9 is calculated by the FDTD method. The result is plotted in Fig. 13. In our calculation, we choose $\Delta x=\Delta y=\Delta=0.05a$ and $\Delta t=0.8\Delta/(c\sqrt{2})$. We have confirmed that no obvious improvement is achieved when higher-resolution meshes are chosen. When $r_1=0.166a$ and $r_2=0.145a$, the peak near $0.29(2\pi c/a)$ corresponds to the cutoff frequency of the air waveguide. The height of this peak decreases when the point P moves from the center of the rod toward the air waveguide. The peak near $0.287(2\pi c/a)$ corresponds to the cutoff frequency of the waveguide (mode 1). The height of this second peak increases when the point P moves from the center of the rod toward the air waveguide. When the point P (indicated in Fig. 9) is away from the

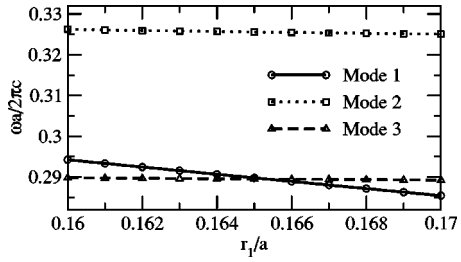

FIG. 12. The dependence of the cutoff frequencies on the rod radius r_1.

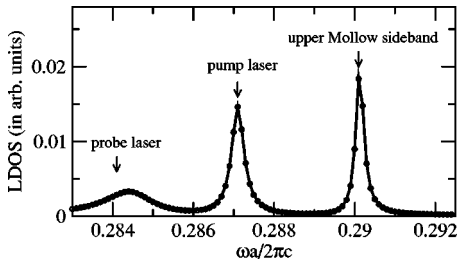

FIG. 13. The local density of states for 2D photonic crystal waveguides with the length $15a$. The radii of rods are $r_0=0.25a$, $r_1=0.166a$, and $r_2=0.145a$, respectively. The dipole is placed at the point P in Fig. 9. To use this waveguide architecture for atomic inversion and switching, pumping laser beams whose frequency coincides with the left LDOS peak are used to drive the upper Mollow sideband of an atom to the peak frequency of the right LDOS peak. Meanwhile, the same pump laser beams drive the lower Mollow sideband of the atom into the low LDOS region to the left of the leftmost LDOS peak. A probe beam whose frequency coincides with the lower Mollow sideband can then be amplified by the inverted atom.

center of the rod by $0.1a$ (toward the air waveguide), those two LDOS peaks have comparable heights. There is a shallow peak near $0.284(2\pi c/a)$. This is also a Fabry-Perot effect due to the finite size of our sample (see Sec. IV). The steady-state pumping laser frequency is adjusted to the left LDOS peak (mode 1), and the higher frequency peak (mode 3) is chosen to coincide with the upper Mollow sideband of the atomic resonances fluorescence spectrum. The probing laser is adjusted to the lower Mollow sideband. Since the probing laser couples to a linear dispersion (high group velocity part) of the second waveguide (mode 2), rapid modulation (or switching) is possible for such an all-optical transistor device.

VI. CONCLUSION

In summary, we have presented a heterostructure consisting of a 2D photonic crystal microchip embedded in a 3D PBG material in which the electromagnetic vacuum LDOS has been engineered with suitable jumps within a narrow range of frequencies in order to implement all-optical switching and transistor action. For a particular 2D microchip architecture, it is possible to create a fork-shaped LDOS, which provides a filter function in the presence of an inhomogeneously broadened "atomic" system. When the length of the waveguide in a 3D heterostructure is $20a$ ($12\ \mu$m), the LDOS can have a jump of an order of 100 within a range of relative frequencies about $10^{-4}\omega_c$, where ω_c is the cutoff frequency of the waveguide mode.

One valuable feature of waveguide structure is that near the waveguide cutoff frequency, the field is almost the same for rods along the waveguide direction. Therefore, atoms that are placed on adjacent rods along the waveguide direction will experience the same coherent field. This facilities very large scale collective response. Collective atomic switching can greatly enhance the optical switching effect. For example, collective response drastically reduces the width of

the switching intensity regime and makes the system much less sensitive to dephasing interactions [8,9,18]. Unlike a collection of atoms that are all confined within a cubic wavelength, a collection of quantum dots that is spread over the length of a 10 microscale waveguide channel is less susceptible to competing effects such as direct resonance dipole-dipole interactions (RDDI). Instead, the "atoms" interact more strongly with the high-intensity peaks of the periodically repeating pump laser field that passes through the waveguide. Other structures such as a single defect (or cavity) may also have a big jump of the LDOS within a small range of frequencies. However, they have little potential to integrate a large number of atoms or quantum dots inside or near the single defect (or cavity). Furthermore, the interaction of the cavity mode with the waveguide mode leads to the conventional tradeoff between switching intensity and switching speed. It would be of considerable interest to simulate in detail the propagation of light in the engineered vacuum of the trimodal waveguide, including the resonant nonlinear dielectric response of the "atomic" system to obtain a full picture of all-optical switching.

ACKNOWLEDGMENTS

We are grateful to Marian Florescu and Ovidiu Toader for some helpful discussions. This work was supported by the Natural Sciences and Engineering Research Council of Canada.

APPENDIX A: FORMULATION OF FIELD-MODE EVALUATION

The Maxwell wave equation in the frequency domain is [23]

$$\boldsymbol{\nabla}\times\left[\frac{1}{\epsilon(\mathbf{r})}\nabla\times\mathbf{H}(\mathbf{r})\right]=\frac{\omega^2}{c^2}\mathbf{H}(\mathbf{r}), \tag{A1}$$

where $\mathbf{H}(\mathbf{r})$ is the divergence-free magnetic field which satisfies $\boldsymbol{\nabla}\cdot\mathbf{H}(\mathbf{r})=0$. In Eq. (A1), the periodic dielectric constant at position $\mathbf{r}$, $\epsilon(\mathbf{r})$, can be written as

$$\epsilon(\mathbf{r})=\sum_{\mathbf{G}}\epsilon(\mathbf{G})e^{i\mathbf{G}\cdot\mathbf{r}}. \tag{A2}$$

Here, $\mathbf{G}$ is a reciprocal-lattice vector. The Fourier coefficients $\epsilon_{\mathbf{G}}$ are given by

$$\epsilon(\mathbf{G})=\frac{1}{\mathcal{V}}\int_{\mathrm{WSC}}d\mathbf{r}\epsilon(\mathbf{r})e^{-i\mathbf{G}\cdot\mathbf{r}}, \tag{A3}$$

where $\mathcal{V}$ is the volume of the Wigner-Seitz cell. The magnetic field can be also expanded as

$$\mathbf{H}(\mathbf{k},\mathbf{r})=\sum_{\mathbf{G}}\sum_{\lambda}h_{\mathbf{G}}^{\lambda}\mathbf{e}_{\mathbf{G}}^{\lambda}e^{i(\mathbf{k}+\mathbf{G})\cdot\mathbf{r}}, \tag{A4}$$

where $\mathbf{e}_{\mathbf{G}}^{\lambda}$ (with $\lambda=1,2$) are two unit vectors perpendicular to $\mathbf{k}+\mathbf{G}$. These three vectors, $\mathbf{e}_{\mathbf{G}}^{1}$, $\mathbf{e}_{\mathbf{G}}^{2}$, and $\mathbf{k}+\mathbf{G}$, form an orthogonal triad. Using Eqs. (A2) and (A4), Eq. (A1) can be rewritten as

$$\sum_{\mathbf{G}'}|\mathbf{k}+\mathbf{G}||\mathbf{k}+\mathbf{G}'|\epsilon^{-1}(\mathbf{G}-\mathbf{G}')\begin{pmatrix}\mathbf{e}_{\mathbf{G}}^{2}\cdot\mathbf{e}_{\mathbf{G}'}^{2} & -\mathbf{e}_{\mathbf{G}}^{2}\cdot\mathbf{e}_{\mathbf{G}'}^{1}\\ -\mathbf{e}_{\mathbf{G}}^{1}\cdot\mathbf{e}_{\mathbf{G}'}^{2} & \mathbf{e}_{\mathbf{G}}^{1}\cdot\mathbf{e}_{\mathbf{G}'}^{1}\end{pmatrix}\begin{pmatrix}h_{\mathbf{G}'}^{1}\\ h_{\mathbf{G}'}^{2}\end{pmatrix}=\frac{\omega^2}{c^2}\begin{pmatrix}h_{\mathbf{G}}^{1}\\ h_{\mathbf{G}}^{2}\end{pmatrix}. \tag{A5}$$

Here, $\epsilon^{-1}(\mathbf{G}-\mathbf{G}')$ is the inverse matrix of $\epsilon(\mathbf{G}-\mathbf{G}')$, whose elements $\epsilon(\mathbf{G},\mathbf{G}')\equiv\epsilon(\mathbf{G}-\mathbf{G}')$ [32]. After the eigenvector of the magnetic field is obtained by diagonalizing Eq. (A5), there are two ways to calculate the electric field from the magnetic field. One is

$$\mathbf{E}(\mathbf{k},\mathbf{r})=\frac{-i}{\omega_n(\mathbf{k})\epsilon_0\epsilon(\mathbf{r})}\boldsymbol{\nabla}\times\mathbf{H}(\mathbf{r})=\frac{1}{\omega_n(\mathbf{k})\epsilon_0\epsilon(\mathbf{r})}\sum_{\mathbf{G}}|\mathbf{k}+\mathbf{G}|\times(h_{\mathbf{G}}^{1}\mathbf{e}_{\mathbf{G}}^{2}-h_{\mathbf{G}}^{2}\mathbf{e}_{\mathbf{G}}^{1})e^{i(\mathbf{k}+\mathbf{G})\cdot\mathbf{r}}; \tag{A6}$$

the other is [25]

$$\mathbf{E}(\mathbf{k},\mathbf{r})=\frac{1}{\omega_n(\mathbf{k})\epsilon_0}\sum_{\mathbf{G},\mathbf{G}'}|\mathbf{k}+\mathbf{G}|\epsilon^{-1}(\mathbf{G}-\mathbf{G}')(h_{\mathbf{G}}^{1}\mathbf{e}_{\mathbf{G}}^{2}-h_{\mathbf{G}}^{2}\mathbf{e}_{\mathbf{G}}^{1})e^{i(\mathbf{k}+\mathbf{G})\cdot\mathbf{r}}. \tag{A7}$$

Equation (A6) is simple. However, due to the Gibbs phenomenon, the results will oscillate near the interface of two different media. On the contrary, Eq. (A7) is complicated and more time-consuming, but the results have no such oscillations near the interface. In this paper, Eq. (A7) is used to calculate the electric-field distribution inside the structure.

APPENDIX B: ELECTROMAGNETIC LDOS OF A FINITE STRUCTURE

When a dipole is placed inside a photonic crystal, the energy emitted by the oscillating dipole is proportional to the LDOS [25]. A similar relation is true when the dipole is placed inside a heterostructure without periodicity. We follow the method described in Ref. [26].

Maxwell's equations are

$$\boldsymbol{\nabla}\cdot\mathbf{D}(\mathbf{r},t)=-\boldsymbol{\nabla}\cdot\mathbf{P}(\mathbf{r},t),$$

$$\boldsymbol{\nabla}\cdot\mathbf{H}(\mathbf{r},t)=0,$$

$$\boldsymbol{\nabla}\times\mathbf{E}(\mathbf{r},t)=-\mu_0\frac{\partial}{\partial t}\mathbf{H}(\mathbf{r},t),$$

$$\nabla \times \mathbf{H}(\mathbf{r},t) = \frac{\partial}{\partial t}[\mathbf{D}(\mathbf{r},t) + \mathbf{P}(\mathbf{r},t)], \tag{B1}$$

where $\mathbf{D}(\mathbf{r},t) = \epsilon_0 \epsilon(\mathbf{r})\mathbf{E}(\mathbf{r},t)$ and $\mathbf{P}(\mathbf{r},t)$ is the extrinsic polarization field. If we define another function

$$\mathbf{Q}(\mathbf{r},t) \equiv \sqrt{\epsilon(\mathbf{r})}\mathbf{E}(\mathbf{r},t) \tag{B2}$$

from Eq. (B1), we have

$$\mathcal{H}\mathbf{Q}(\mathbf{r},t) = -\frac{1}{c^2}\frac{\partial^2}{\partial t^2}\mathbf{Q}(\mathbf{r},t) - \frac{1}{c^2\epsilon_0\sqrt{\epsilon(\mathbf{r})}}\frac{\partial^2}{\partial t^2}\mathbf{P}(\mathbf{r},t), \tag{B3}$$

where $\mathcal{H}$ is a Hermitian operator defined by

$$\mathcal{H}\mathbf{Q}(\mathbf{r},t) \equiv \frac{1}{\sqrt{\epsilon(\mathbf{r})}}\nabla \times \left(\nabla \times \frac{1}{\sqrt{\epsilon(\mathbf{r})}}\mathbf{Q}(\mathbf{r},t)\right). \tag{B4}$$

When there is no extrinsic polarization, i.e., $\mathbf{P}(\mathbf{r},t)=0$, Eq. (B3) becomes

$$\frac{1}{c^2}\frac{\partial^2}{\partial t^2}\mathbf{Q}(\mathbf{r},t) + \frac{1}{\sqrt{\epsilon(\mathbf{r})}}\nabla \times \left(\nabla \times \frac{1}{\sqrt{\epsilon(\mathbf{r})}}\mathbf{Q}(\mathbf{r},t)\right) = \mathbf{0}. \tag{B5}$$

Suppose the function $\mathbf{Q}(\mathbf{r},t)$ has the form $e^{-i\omega t}$. Then,

$$\frac{1}{\sqrt{\epsilon(\mathbf{r})}}\nabla \times \left(\nabla \times \frac{1}{\sqrt{\epsilon(\mathbf{r})}}\mathbf{Q}_n(\mathbf{r})\right) = \frac{\omega_n^2}{c^2}\mathbf{Q}_n(\mathbf{r}). \tag{B6}$$

There are two kinds of solutions for Eq. (B6). The first kind are quasilongitudinal solutions, which have zero eigenvalues, i.e., $(\omega_n=0)$. Then, Eq. (B6) becomes

$$\nabla \times \left(\frac{1}{\sqrt{\epsilon(\mathbf{r})}}\mathbf{Q}_n^{(L)}(\mathbf{r})\right) = \mathbf{0}. \tag{B7}$$

These solutions are not propagating waves because the corresponding eigenfrequencies are zero [see Eq. (B6)]. However, these solutions are important mathematically because they are needed to construct a complete set of the eigensolutions. The second kind are quasitransverse solutions, which have nonzero eigenvalues,

$$\frac{1}{\sqrt{\epsilon(\mathbf{r})}}\nabla \times \left(\nabla \times \frac{1}{\sqrt{\epsilon(\mathbf{r})}}\mathbf{Q}_n^{(T)}(\mathbf{r})\right) = \frac{\omega_n^{(T)2}}{c^2}\mathbf{Q}_n^{(T)}(\mathbf{r}). \tag{B8}$$

The eigenfunctions are renormalized as the following:

$$\int_{\mathcal{V}} \mathbf{Q}_n^{\alpha *}(\mathbf{r}) \cdot \mathbf{Q}_{n'}^{\beta}(\mathbf{r}) = \mathcal{V}\delta_{\alpha\beta}\delta_{nn'}, \tag{B9}$$

where $\alpha(\beta)=T(L)$, and $\mathcal{V}$ is the volume of the system. The completeness of the eigenfunction leads to

$$\sum_n \mathbf{Q}_n^{(T)}(\mathbf{r}) \otimes \mathbf{Q}_n^{(T)*}(\mathbf{r}') + \sum_n \mathbf{Q}_n^{(L)}(\mathbf{r}) \otimes \mathbf{Q}_n^{(L)*}(\mathbf{r}') = \mathcal{V}I\delta(\mathbf{r} - \mathbf{r}'), \tag{B10}$$

where $\otimes$ is an operation that results in a tensor from two vectors, i.e., $(A \otimes B)_{ij} = A_i B_j$, and I is the unit tensor.

A retarded Green's (tensor) function $G(\mathbf{r},\mathbf{r}',t)$ satisfies the following equations:

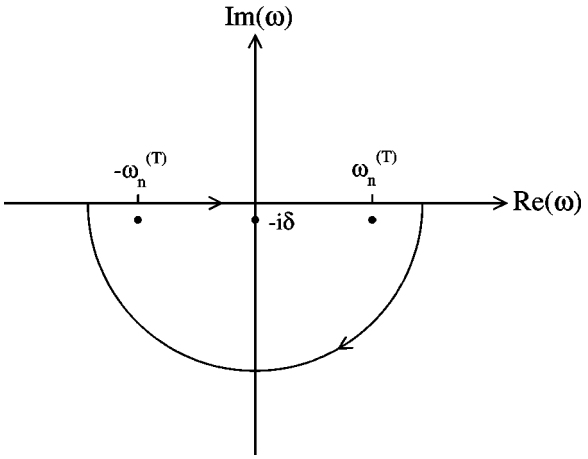

FIG. 14. The integration contour C in Eq. (B15).

$$-\left(\frac{1}{c^2}\frac{\partial^2}{\partial t^2} + \mathcal{H}\right)G(\mathbf{r},\mathbf{r}',t-t') = I\delta(\mathbf{r}-\mathbf{r}')\delta(t-t'),$$

$$G(\mathbf{r},\mathbf{r}',t) = 0 \quad \text{for} \quad t < 0. \tag{B11}$$

The Green's function in frequency space $\mathcal{G}(\mathbf{r},\mathbf{r}',\omega)$ is defined by the Fourier transform of $G(\mathbf{r},\mathbf{r}',t)$,

$$G(\mathbf{r},\mathbf{r}',t) \equiv \frac{1}{2\pi}\int_{-\infty}^{\infty} d\omega \mathcal{G}(\mathbf{r},\mathbf{r}',\omega)e^{-i\omega t}. \tag{B12}$$

Then, $\mathcal{G}(\mathbf{r},\mathbf{r}',\omega)$ satisfies the following equation:

$$\left(\frac{\omega^2}{c^2} - \mathcal{H}\right)\mathcal{G}(\mathbf{r},\mathbf{r}',\omega) = I\delta(\mathbf{r}-\mathbf{r}'). \tag{B13}$$

From Eqs. (B7), (B8), (B10), and (B13), we have

$$\mathcal{G}(\mathbf{r},\mathbf{r}',\omega) \equiv \int_{-\infty}^{\infty} dt G(\mathbf{r},\mathbf{r}',t)e^{i\omega t} = \frac{c^2}{\mathcal{V}}\sum_n \left(\frac{\mathbf{Q}_n^{(T)}(\mathbf{r}) \otimes \mathbf{Q}_n^{(T)*}(\mathbf{r}')}{(\omega - \omega_n^{(T)} + i\delta)(\omega + \omega_n^{(T)} + i\delta)} + \frac{\mathbf{Q}_n^{(L)}(\mathbf{r}) \otimes \mathbf{Q}_n^{(L)*}(\mathbf{r}')}{(\omega + i\delta)^2}\right), \tag{B14}$$

where δ is a positive infinitesimal. For $t \geq 0$, the inverse transform of Eq. (B14) gives

$$G(\mathbf{r},\mathbf{r}',t)=\frac{c^2}{2\pi\mathcal{V}}\sum_n\frac{\mathbf{Q}_n^{(T)}(\mathbf{r})\otimes\mathbf{Q}_n^{(T)*}(\mathbf{r}')}{2\omega_n^{(T)}}\int_C d\omega\left(\frac{1}{\omega-\omega_n^{(T)}+i\delta}-\frac{1}{\omega+\omega_n^{(T)}+i\delta}\right)e^{-i\omega t}$$
$$+\frac{c^2}{2\pi\mathcal{V}}\sum_n\mathbf{Q}_n^{(L)}(\mathbf{r})\otimes\mathbf{Q}_n^{(L)*}(\mathbf{r}')\int_C d\omega\frac{e^{-i\omega t}}{(\omega+i\delta)^2}=-\frac{c^2}{\mathcal{V}}\sum_n\left(\frac{\sin\omega_n^{(T)}t}{\omega_n^{(T)}}\mathbf{Q}_n^{(T)}(\mathbf{r})\otimes\mathbf{Q}_n^{(T)*}(\mathbf{r}')+t\mathbf{Q}_n^{(L)}(\mathbf{r})\otimes\mathbf{Q}_n^{(L)*}(\mathbf{r}')\right), \tag{B15}$$

where C is the integration contour shown in Fig. 14. The solution of Eq. (B3) can be obtained by a convolution integral of the Green's function,

$$\mathbf{Q}(\mathbf{r},t)=\int_{\mathcal{V}}d\mathbf{r}'\int_{-\infty}^{\infty}dt'G(\mathbf{r},\mathbf{r}',t-t)\frac{1}{c^2\epsilon_0\sqrt{\epsilon(\mathbf{r}')}}\frac{\partial^2}{\partial t^2}\mathbf{P}(\mathbf{r}',t')$$
$$=-\frac{1}{\epsilon_0\mathcal{V}}\sum_n\int_{\mathcal{V}}d\mathbf{r}'\int_{-\infty}^{t}dt'\left(\frac{\sin\omega_n^{(T)}(t-t')}{\omega_n^{(T)}}\mathbf{Q}_n^{(T)}(\mathbf{r})\otimes\mathbf{Q}_n^{(T)*}(\mathbf{r}')+(t-t')\mathbf{Q}_n^{(L)}(\mathbf{r})\otimes\mathbf{Q}_n^{(L)*}(\mathbf{r}')\right)\frac{1}{\sqrt{\epsilon(\mathbf{r}')}}\frac{\partial^2}{\partial t^2}\mathbf{P}(\mathbf{r}',t'), \tag{B16}$$

where the extrinsic polarization $\mathbf{P}(\mathbf{r},t)$ is assumed to be introduced adiabatically, i.e., $\mathbf{P}(\mathbf{r},-\infty)=0$. Carrying out the t' integral by parts, we obtain

$$\mathbf{Q}(\mathbf{r},t)=-\frac{1}{\epsilon_0\mathcal{V}}\sum_n\int_{\mathcal{V}}d\mathbf{r}'\int_{-\infty}^{t}dt'[\cos\omega_n^{(T)}(t-t')\mathbf{Q}_n^{(T)}(\mathbf{r})\otimes\mathbf{Q}_n^{(T)*}(\mathbf{r}')+\mathbf{Q}_n^{(L)}(\mathbf{r})\otimes\mathbf{Q}_n^{(L)*}(\mathbf{r}')]\frac{1}{\sqrt{\epsilon(\mathbf{r}')}}\frac{\partial}{\partial t}\mathbf{P}(\mathbf{r}',t')$$
$$=-\frac{1}{\epsilon_0\mathcal{V}}\sum_n\int_{\mathcal{V}}d\mathbf{r}'[\mathbf{Q}_n^{(T)}(\mathbf{r})\otimes\mathbf{Q}_n^{(T)*}(\mathbf{r}')+\mathbf{Q}_n^{(L)}(\mathbf{r})\otimes\mathbf{Q}_n^{(L)*}(\mathbf{r}')]\frac{1}{\sqrt{\epsilon(\mathbf{r}')}}\mathbf{P}(\mathbf{r}',t)$$
$$+\frac{1}{\epsilon_0\mathcal{V}}\sum_n\int_{\mathcal{V}}d\mathbf{r}'\int_{-\infty}^{t}dt'\left(\omega_n^{(T)}\sin\omega_n^{(T)}(t-t')\mathbf{Q}_n^{(T)}(\mathbf{r})\otimes\mathbf{Q}_n^{(T)*}(\mathbf{r}')\right)\frac{1}{\sqrt{\epsilon(\mathbf{r}')}}\mathbf{P}(\mathbf{r}',t')$$
$$=-\frac{\mathbf{P}(\mathbf{r},t)}{\epsilon_0\sqrt{\epsilon(\mathbf{r})}}+\frac{1}{\epsilon_0\mathcal{V}}\sum_n\mathbf{Q}_n^{(T)}(\mathbf{r})\int_{\mathcal{V}}d\mathbf{r}'\int_{-\infty}^{t}dt'\frac{\mathbf{Q}_n^{(T)*}(\mathbf{r}')\cdot\mathbf{P}(\mathbf{r}',t')}{\sqrt{\epsilon(\mathbf{r}')}}\omega_n^{(T)}\sin\omega_n^{(T)}(t-t'). \tag{B17}$$

Replacing the function $\mathbf{Q}$ by the electric field $\mathbf{E}$, we finally obtain Eq. (B18),

$$\mathbf{E}(\mathbf{r},t)+\frac{\mathbf{P}(\mathbf{r},t)}{\epsilon_0\epsilon(\mathbf{r})}=\frac{1}{\epsilon_0\mathcal{V}}\sum_n\mathbf{E}_n^{(T)}(\mathbf{r})\int_{\mathcal{V}}d\mathbf{r}'\int_{-\infty}^{t}dt'\mathbf{E}_n^{(T)*}(\mathbf{r}')\cdot\mathbf{P}(\mathbf{r}',t')\omega_n^{(T)}\sin\omega_n^{(T)}(t-t'), \tag{B18}$$

where $\mathbf{E}_n^{(T)}(\mathbf{r},t)$ are quasitransverse solutions of Eq. (B1) with eigenfrequency ω_n when the extrinsic polarization $\mathbf{P}(\mathbf{r},t)=0$. If the dipole oscillates with frequency ω at $\mathbf{r}_0$, the extrinsic polarization will be

$$\mathbf{P}(\mathbf{r},t)=\mathbf{d}\delta(\mathbf{r}-\mathbf{r}_0)e^{(-i\omega+\delta)t}, \tag{B19}$$

where $\mathbf{d}$ is the dipole moment and δ is a positive infinitesimal. The function $e^{\delta t}$ is used to obtain an adiabatic switching for the extrinsic polarization. Inserting Eq. (B19) into Eq. (B18), we have

$$\mathbf{E}(\mathbf{r},t)+\frac{\mathbf{P}(\mathbf{r},t)}{\epsilon_0\epsilon(\mathbf{r})}=\frac{e^{-i\omega t}}{2\epsilon_0\mathcal{V}}\sum_n\omega_n^{(T)}\mathbf{E}_n^{(T)}(\mathbf{r})[\mathbf{E}_n^{(T)*}(\mathbf{r}_0)\cdot\mathbf{d}]\left(\frac{1}{\omega+\omega_n^{(T)}+i\delta}-\frac{1}{\omega-\omega_n^{(T)}+i\delta}\right). \tag{B20}$$

The energy emitted by the dipole is characterized by Poynting's vector,

$$\mathbf{S}(\mathbf{r},t)=[\mathbf{E}(\mathbf{r},t)+\mathbf{E}^*(\mathbf{r},t)]\times[\mathbf{H}(\mathbf{r},t)+\mathbf{H}^*(\mathbf{r},t)]. \tag{B21}$$

The time-averaged Poynting vector $\overline{\mathbf{S}(\mathbf{r},t)}$ is

$$\overline{\mathbf{S}(\mathbf{r},t)}=\overline{[\mathbf{E}(\mathbf{r},t)+\mathbf{E}^*(\mathbf{r},t)]\times[\mathbf{H}(\mathbf{r},t)+\mathbf{H}^*(\mathbf{r},t)]}. \tag{B22}$$

Since both $\mathbf{E}$ and $\mathbf{H}$ are proportional to $e^{-i\omega t}$, the time-averaged Poynting vector can be simplified as

$$\overline{\mathbf{S}(\mathbf{r},t)}=[\mathbf{E}(\mathbf{r},t)\times\mathbf{H}^*(\mathbf{r},t)]+[\mathbf{E}^*(\mathbf{r},t)\times\mathbf{H}(\mathbf{r},t)]. \tag{B23}$$

Taking the divergence of both sides of Eq. (B23), we have

$$\nabla \cdot \overline{\mathbf{S}(\mathbf{r},t)} = \{\mathbf{H}^*(\mathbf{r},t)\cdot[\nabla\times\mathbf{E}(\mathbf{r},t)] - \mathbf{E}(\mathbf{r},t)\cdot[\nabla\times\mathbf{H}^*(\mathbf{r},t)] + \mathbf{H}(\mathbf{r},t)\cdot[\nabla\times\mathbf{E}^*(\mathbf{r},t)] - \mathbf{E}^*(\mathbf{r},t)\cdot[\nabla\times\mathbf{H}(\mathbf{r},t)]\}$$
$$= i\omega[\mathbf{E}^*(\mathbf{r},t)\cdot\mathbf{P}(\mathbf{r},t) - \mathbf{E}(\mathbf{r},t)\cdot\mathbf{P}^*(\mathbf{r},t)]. \quad \text{(B24)}$$

Substituting Eqs. (B19) and (B20) into Eq. (B24) and using the identity

$$\frac{1}{\omega-\omega_0\pm i\delta} = \mathrm{P}\frac{1}{\omega-\omega_0} \mp \pi i\delta(\omega-\omega_0), \quad \text{(B25)}$$

where P denotes principal value, we have

$$\nabla\cdot\overline{\mathbf{S}(\mathbf{r},t)} = \frac{\pi\omega^2}{\epsilon_0\mathcal{V}}\delta(\mathbf{r}-\mathbf{r}_0)\sum_n |\mathbf{d}\cdot\mathbf{E}_n^{(T)*}(\mathbf{r}_0)|^2\delta(\omega-\omega_n^{(T)}). \quad \text{(B26)}$$

If the volume containing the dipole is denoted as $\mathcal{V}_1$ and the corresponding bounding surface is denoted as S_1, the energy U emitted by the dipole is given by the surface integral of the surface normal component of Poynting's vector, $S_n \equiv \mathbf{S}\cdot\hat{n}$ ($\hat{n}$ is a unit vector normal to S_1),

$$U = \int_{S_1} dS\overline{\mathbf{S}_n(\mathbf{r},t)} = \int_{\mathcal{V}_1} d\mathbf{r}\,\nabla\cdot\overline{\mathbf{S}(\mathbf{r},t)}$$
$$= \frac{\pi\omega^2}{\epsilon_0\mathcal{V}}\sum_n |\mathbf{d}\cdot\mathbf{E}_n^{(T)*}(\mathbf{r}_0)|^2\delta(\omega-\omega_n^{(T)}). \quad \text{(B27)}$$

The LDOS is defined as

$$\rho(\omega,\mathbf{r}_0) = \frac{1}{\mathcal{V}d_0^2}\sum_n |\mathbf{d}\cdot\mathbf{E}_n^{(T)*}(\mathbf{r}_0)|^2\delta(\omega-\omega_n^{(T)}), \quad \text{(B28)}$$

where d_0 is the magnitude of the dipole moment **d**. From Eqs. (B27) and (B28), we have

$$\rho(\omega,\mathbf{r}_0) = \frac{\epsilon_0}{\pi\omega^2 d_0^2}U. \quad \text{(B29)}$$

[1] S. John, Phys. Rev. Lett. **53**, 2169 (1984); **58**, 2486 (1987).
[2] E. Yablonovitch, Phys. Rev. Lett. **58**, 2059 (1987).
[3] For a recent review, see articles in *Photonic Crystals and Localization in the 21st Century*, edited by C. M. Soukoulis (Kluwer, Dordrecht, 2001); J. Lightwave Technol. **17**, No. 11 (1999).
[4] A. Blanco, E. Chomski, S. Grabtchak, M. Ibisate, S. John, S. W. Leonard, C. Lopez, F. Meswguer, H. Miguez, J. P. Mondia, G. A. Ozin, O. Toader, and H. M. van Driel, Nature (London) **405**, 437 (2000).
[5] S. John and J. Wang, Phys. Rev. Lett. **64**, 2418 (1990); Phys. Rev. B **43**, 12 772 (1991).
[6] M. Florescu and S. John, Phys. Rev. A **64**, 033801 (2001).
[7] R. Loudon, *The Quantum Theory of Light* (Oxford University Press, Oxford, 2000).
[8] S. John and T. Quang, Phys. Rev. Lett. **78**, 1888 (1997).
[9] S. John and M. Florescu, J. Opt. A, Pure Appl. Opt. **3**, S103 (2001).
[10] H. M. Gibbs, *Optical Bistability: Controlling Light with Light* (Academic Press, New York, 1985).
[11] H. M. Gibbs, S. L. McCall, and T. N. C. Venkatesan, Phys. Rev. Lett. **36**, 1135 (1976).
[12] M. Soljačić, M. Ibanescu, S. G. Johnson, Y. Fink, and J. D. Joannopoulos, Phys. Rev. E **66**, 055601 (2002); M. F. Yanik, S. Fan, and M. Soljačić, Appl. Phys. Lett. **83**, 2739 (2003).
[13] P. St. Russell, IEEE J. Quantum Electron. **31**, 673 (1991); Electron. Lett. **29**, 1228 (1993).
[14] D. A. B. Miller, *in Optical Computing: Proceedings of the Thirty-fourth Scottish Universities Summer School in Physics, Heriot-Watt University, Edinburgh, 1988*, edited by B. S. Wherrett and F. A. P. Tooley (Edinburgh, Scotland, 1989).
[15] P. Lambropoulos, G. M. Nikolopoulos, T. R. Nielsen, and S. Bay, Rep. Prog. Phys. **63**, 455 (2000).
[16] D. Kleppner, Phys. Rev. Lett. **47**, 233 (1981).
[17] S. John and T. Quang, Phys. Rev. Lett. **74**, 3419 (1995).
[18] M. Florescu and S. John, Phys. Rev. A **69**, 053810 (2004).
[19] R. L. Williams, G. C. Aers, P. J. Poole, J. Lefebvre, D. Chithrani, and B. Lamontagne, J. Cryst. Growth **223**, 321 (2001); J. Lefebvre, P. J. Poole, J. Fraser, G. C. Aers, D. Chithrani, and R. L. Williams, *ibid.* **234**, 391 (2002).
[20] A. Chutinan, S. John, and O. Toader, Phys. Rev. Lett. **90**, 123901 (2003).
[21] M. Florescu, Ph.D. thesis, University of Toronto, 2002.
[22] R. D. Meade, A. Devenyi, J. D. Joannopoulos, O. L. Alerhand, D. A. Smith, and K. Kash, J. Appl. Phys. **75**, 4753 (1994); J. D. Joannopoulos, P. R. Villeneuve, and S. Fan, Nature (London) **386**, 143 (1997); A. Mekis, J. C. Chen, I. Kurland, S. Fan, P. R. Villeneuve, and J. D. Joannopoulos, Phys. Rev. Lett. **77**, 3787 (1996); S. Y. Lin, E. Chow, V. Hietala, P. R. Villeneuve, and J. D. Joannopoulos, Science **282**, 274 (1998).
[23] K. M. Leung and Y. F. Liu, Phys. Rev. Lett. **65**, 2646 (1990).
[24] E. Yablonovitch, T. J. Gmitter, R. D. Meade, A. M. Rappe, K. D. Brommer, and J. D. Joannopoulos, Phys. Rev. Lett. **67**, 3380 (1991).
[25] T. Suzuki and P. K. L. Yu, J. Opt. Soc. Am. B **12**, 570 (1995).
[26] K. Sakoda, *Optical Properties of Photonic Crystals* (Springer, Berlin, 2001).
[27] J. K. Hwang, H. Y. Ryu, and Y. H. Lee, Phys. Rev. B **60**, 4688 (1999); Y. Xu, R. K. Lee, and A. Yariv, Phys. Rev. A **61**, 033807 (2000); R. K. Lee, Y. Xu, and A. Yariv, J. Opt. Soc. Am. B **17**, 1438 (2000); C. Hermann and O. Hess, *ibid.* **19**, 3013 (2002).

[28] A. Taflove and S. C. Hagness, *Computational Electrodynamics: The Finite-Difference Time-Domain Method*, 2nd ed. (Artech House, Boston, 2000).

[29] O. Toader and S. John, Science **292**, 1133 (2001); O. Toader and S. John, Phys. Rev. E **66**, 016610 (2002).

[30] S. Y. Lin, J. G. Fleming, D. L. Hetherington, B. K. Smith, R. Biswas, K. M. Ho, M. M. Sigalas, W. Zubrzycki, S. R. Kurtz, and J. Bur, Nature (London) **394**, 251 (1998); S. Noda, K. Tomoda, N. Yamamoto, and A. Chutinan, Science **289**, 604 (2000).

[31] O. Toader, M. Berciu, and S. John, Phys. Rev. Lett. **90**, 233901 (2003).

[32] K. M. Ho, C. T. Chan, and C. M. Soukoulis, Phys. Rev. Lett. **65**, 3152 (1990).

[33] B. W. Shore, *The Theory of Coherent Atomic Excitation* (Wiley, New York, 1990).

[34] G. Mur, IEEE Trans. Electromagn. Compat. **EMC-23**, 377 (1981).